High Pressure CO_2 Photoreduction using Au/TiO_2: unravelling the effect of the co-catalyst and of the titania polymorph

Elnaz Bahdori [a], Antonio Tripodi[a], Alberto Villa [a], Carlo Pirola [a], Laura Prati [a], Gianguido Ramis [b], Nikolaos Dimitratos [c], Di Wang [d], Ilenia Rossetti [a,*]

[a] Dip. Chimica, Università degli Studi di Milano, INSTM Unit Milano-Università and CNR-ISTM, via C. Golgi, 19, I-20133 Milano

[b] Dip. di Ingegneria Civile, Chimica e Ambientale, Università degli Studi di Genova and INSTM Unit Genova, via all'Opera Pia 15A, I-16100, Genoa, Italy

[c] Cardiff Catalysis Institute, School of Chemistry, Cardiff University, Main Building, Park Place, Cardiff, CF103AT, UK. Cardiff University

[d] Institute of Nanotechnology and Karlsruhe Nano Micro Facility (KNMF), Karlsruhe Institute of Technology, Hermann-von-Helmholtz-Platz 1, 76344 Eggenstein-Leopoldshafen, Germany

Abstract

A series of Au/TiO_2 based catalysts with low gold loading (0.1–0.5 wt%) were prepared by a modified deposition–precipitation method and their activity was tested for CO_2 photoreduction in liquid phase

* Corresponding author: Fax +39-02-50314300; email ilenia.rossetti@unimi.it

at high pressure (7 bar). Methanol, formic acid and formaldehyde were detected as major products in liquid phase, whilst gas phase products, CO, CH_4 and H_2 were produced in different concentration depending on catalyst formulation. The deposition of small Au nanoparticles (3-5 nm) (NPs) onto TiO_2 was found to quantitatively influence the products distribution and the productivities of various products. Characterization techniques, such as DRIFTS, XRD and TEM/HAADF were used to correlate the photocatalyst features with the photoactivity obtained. Methanol productivity of 1360 and 1350 mmol kg_{cat}^{-1} h^{-1} were attained for 0.2 wt% Au/TiO_2 and 0.5 wt% Au/TiO_2, respectively, which are impressive results with respect to the literature. However, the highest loaded sample revealed simultaneously the highest H_2 and CH_4 productivities. By contrast, lower activity was obtained using anatase and rutile pure phases, with respect to the mixed phase P25 commercial sample, confirming the key role of interfacial defects between borders of different crystalline phases.

Keywords: CO_2 reduction; Photoreduction; Photoreactor; Gold; Titania; Photocatalysis; High pressure photocatalysis.

1 - Introduction

The Earth's surface temperature has continuously risen in the past century, with particularly significant warming trends over the past two decades [1]. CO_2 emissions from fossil sources is believed the primary anthropogenic contributor to this phenomenon. The reduction of CO_2 emissions can be achieved by three approaches: i) efficient use of carbon-based energy sources (energy efficiency concept); ii) use of alternative or carbon-free energy sources (*e.g.* hydrogen obtained by wind/solar energy); iii) post-treatment processes. Within the last option lies the carbon-capture and storage technologies (CCS) and the further CO_2 conversion to chemicals or fuels [2]. This last approach can be a turning point, able to change the carbon dioxide image from a critical waste with a cost of disposal,

to a resource and a business opportunity, with also benefits in terms of positive image for companies. The post-treatment conversion of carbon dioxide can be performed on high purity gas streams from current and planned CSS plants or directly at the outlet of the emission source, especially where CSS option is unsuitable (due to the distance from safe sequestration sites or diluted concentration of CO_2 in the emitting gas or small-medium size sources).

CO_2 is a relatively inert and stable compound, therefore its reduction is very challenging. In particular, the CO_2 reduction by H_2O to form hydrocarbons is an uphill, strongly endothermic process, requiring a considerable amount of energy [3]:

$CO_2 + 2\ H_2O \rightarrow CH_3OH + 3/2\ O_2$ (ΔG_0= +702.2 kJ mol^{-1})

$CO_2 + 2\ H_2O \rightarrow CH_4 + 2\ O_2$ (ΔG_0= +818.3 kJ mol^{-1})

The recent innovations in photocatalytic technologies have introduced CO_2 photo-conversion to fuels and chemicals as a tangible future alternative [4–6]. Direct conversion of CO_2 under light irradiation is possible only using artificial light because of the absorption below 200 nm in the so-called deep UV region [7]. However, using a photo-catalyst, UV and solar sources can be used under milder conditions, as recently reviewed[8,9]. The photo-catalyst plays a crucial role because of the generation of active charged species (electrons and holes) upon light absorption [10]. These species are very active and can convert the chemical compounds adsorbed on the material or lying around it. Among the various semiconductors usable as photocatalysts, TiO_2 is widely used because of its low toxicity, low cost and photo-corrosion resistance.

Titania has three polymorph forms: anatase, rutile and brookite. Among these, anatase is the most photocatalytically active form, though not for all applications [11]. It also has a slightly larger band gap compared to rutile and brookite (3.2, 3.0 and 3.1 eV respectively). However, there is not univocal interpretation on the activity of the different crystal phases. The role of the TiO_2 structure in

photocatalysis has been recently reviewed [12,13] highlighting the effect of crystal phases and co-catalysts, often in connection.

The drawbacks of bare TiO_2 are the high electron–hole recombination rate and the limited absorption in the visible region. An attractive method to improve these limitations is the modification of TiO_2 by means of non-metal elements or deposition of surface metallic nanoparticles [14]. The influence of the promoter or co-catalyst is very different in these two cases. Doping involves the incorporation of atoms or ions in the crystalline oxide lattice, although the real location of the hetero-atoms is not always clear [15]. For instance Olivo et al. designed several N doped CuO-TiO_2 photocatalysts studying the co-promotion effect on the photoreduction process [16]. C-doping and the development of heterojunctions is another important strategy[17–21].

On the other hand, deposition of metallic nanoparticles, such as Pt [22], Pd [14], Ag [23] and Au [24], Co[25] onto TiO_2 surface could enhance the photocatalytic activity by suppressing significantly the electron-hole recombination due to the formation of a Schottky barrier at the interface between the metal and support. Since the TiO_2 conduction band is essentially formed by the overlapping of Ti 3d orbitals, the presence of the metal introduces an empty *d* orbital below the conduction band edge causing the effective band gap reduction and acting as charge carrier trap.

In our previous investigations we have described a new photoreactor concept which can operate up to 20 bar [26–28]. We have demonstrated that the photoreduction of CO_2 in gas phase is less productive than in three-phase gas/liquid/solid configuration [16,29] and that the increase of CO_2 pressure can increase its solubility and adsorption over the catalyst, also allowing a considerable increase of the working temperature [27,28,30]. The role of pH has been also addressed, leading to two different reaction pathways, summarized in the following [30].

In this work, a modified deposition-precipitation method was selected for the preparation of photocatalysts for the reduction of CO_2. The method involves the use of urea as basic agent and $NaBH_4$ as chemical reductant in contrast to the traditional high-temperature reduction step. In this

way, highly dispersed gold nanoparticles can be obtained at very low metal loading, in a metallic form with a partial negative charge [31]. Low metal loading (0.1-0.5 wt%) was chosen to avoid excessive surface coverage and relative inhibition of substrate adsorption, but maintaining visible light absorption properties and enhanced electron-hole separation after the photo-generation.

The materials were fully characterized [32] and here tested for the CO_2 photo-reduction in liquid phase at high pressure (7 bar or higher). This represents a new, unconventional approach to the reaction, with a substantial improvement of the productivity towards both liquid and gas phase products with respect to conventional ambient conditions. We have previously demonstrated that pressure higher than ambient allows a substantial improvement of CO_2 solubility and permits to operate at higher temperature than conventional [29,33–35]. Much higher productivity has been reported even by using a bare TiO_2 photocatalyst for this application than literature reports, which may represent an important step towards the commercialization of this technology [36–38].

This high pressure photoreactor was successfully tested and the CO_2 photoreaction mechanism was deepened over the un-promoted TiO_2 P25 catalyst. The present results shed light on the beneficial effect of Au nanoparticles in boosting the productivity to methanol and other regenerated fuels and chemicals. Indeed, Au nanoparticles already demonstrated very active as co-catalysts for this application. We here deepened their application under unconventional reaction conditions to boost the productivity of all the detected products.

2 - Experimental

2.1. Preparation of Au/TiO_2

Gold nanoparticles were prepared by a modified deposition-precipitation method using urea and a chemical reductant (DP-UC). 1 g of commercial TiO_2 (Evonik P25, 50 m^2 g^{-1}) was dispersed in distilled water (100ml) with 5 g of urea (Aldrich, >99%). $NaAuCl_4 \cdot 2H_2O$ solution (Aldrich, 99.99%)

was added to the support and left under vigorous stirring for 4 h at 353 K. The catalyst was filtered and washed several times with water. The material was then suspended in distilled water and a freshly prepared solution 0.1 M of $NaBH_4$ (Fluka, > 96%) was added ($NaBH_4$/Au = 4 mol/mol) under vigorous stirring at room temperature. The sample was filtered, washed and dried at 373 K for 4 h. The actual Au loading was checked by Atomic Absorption Spectroscopy (AAS) analysis of the filtrate, on a Perkin Elmer 3100 instrument. As expected using this method [39], all the gold present in the solution was deposited on the support. The nominal composition was also confirmed by EDX analysis. Au/P25 catalysts with the following composition were prepared: 0.1 wt%, 0.2 wt%, 0.5 wt% Au/P25. Bare P25 was used as comparative reference. Using the same methodology 0.5 wt% Au/Rutile (Rutile, Aldrich, 99.99% purity) and 0.5 wt%/anatase (Anatase, Aldrich, 99.80% purity) were prepared.

2.2. Characterization

DRIFTS studies were carried out with a Bruker Tensor 27 spectrometer fitted with a HgCdTe (MCT) detector, a Harrick Praying Mantis HVC-DRP-4 cell equipped with two ZnSe windows, and operated with OPUS software. The DRIFTS cell included gas inlet and outlet ports as well as capabilities for heating and cooling. The required gas flow, 40 cm^3 min^{-1} of a 5% CO/N_2 gas mixture was controlled by mass-flow controllers. The data are reported in the form of absorbance. Each spectrum represents an average of 64 scans collected with a spectral resolution of 2 cm^{-1}. The ZnSe windows in use cut off the spectrum below 650 cm^{-1} therefore this region was not included in the discussion. In the reported spectra, a positive increase of peak intensity indicates an increase of population of that species, whereas a negative deflection shows loss of moieties associated with that particular mode. All samples were ground before the analysis. Background subtraction and normalization of the spectra were performed by subtracting (deducing) spectra recorded under N_2 flow (40 cm^3 min^{-1}) after heating the sample at 393K for 30 min, to eliminate physisorbed and chemisorbed moisture.

Specific surface area and pore size distribution were evaluated through the collection of N_2 adsorption-desorption isotherms at 77K on a Micromeritics ASAP 2020 instrument. Surface area was calculated on the basis of the Brunauer, Emmet and Teller equation (BET), whereas the pores size distribution was determined by the BJH method, applied to the N_2 desorption branch of the isotherm. Prior to the analysis the samples were outgassed at 573K for 24 hours.

The specimens for Transmission Electron Microscopy (TEM) were prepared by dispersing the catalyst powder on TEM grids coated with holey carbon film. They were examined by means of a FEI Titan 80–300 electron microscope equipped with CEOS image spherical aberration corrector, Fischione model 3000 high angle annular dark field (HAADF) scanning transmission electron microscopy (STEM) detector.

X-ray diffraction (XRD) experiments were performed on a Rigaku D III-MAX horizontal-scan powder diffractometer with Cu-Kα radiation, equipped with a graphite monochromator on the diffracted beam. The crystallite size was estimated from peak half width by using the Scherrer equation with corrections for instrumental line broadening ($\beta = 0.9$).

X-ray photoelectron spectroscopy (XPS) was carried out with a Kratos (Manchester, M17 1GP, UK) Axis Ultra-DLD instrument with a monochromatic Al K_ X-ray source (144 W, 12 mA, 12 kV). High resolution and survey scans were performed at pass energies of 40 and 160 eV, respectively. Spectra were calibrated to the C (1s) signal at 284.8 eV and quantified using CasaXPS and a modified Wagner sensitivity factors supplied by the manufacturer

2.3. Photo-catalytic testing: CO_2 reduction

The innovative photoreactor used for activity testing has been described in detail elsewhere [33,34]. Briefly, the photo-reactor is made of AISI 316 stainless steel. The lamp is introduced vertically in reactor axis and a magnetic stirrer ensures proper liquid mixing. The internal capacity is *ca.* 1.3 L,

filled with *ca.* 1.2 L solution. The temperature is kept constant through a double-walled thermostatic system.

As source of radiation, we used a medium-pressure Hg vapor lamp with a range of emission wavelengths from 254 nm to 364 nm (this latter was the main peak). The emitted power was periodically measured by means of a photo-radiometer (Delta OHM HD2102,2) at 315-400 nm. At the bottom of the quartz candle, where is located most of the suspension, the power was 45 W m^{-2} at 13.5 cm from the side of the lamp and 77 W m^{-2} at 6 cm under the bulb. The harmful overheat of the lamp bulb was avoided thanks to an air circulation system. The irradiation power depends on the flow rate of the cooling pressurized air, therefore a compromise between the high irradiation power and high lamp lifetime was chosen and corresponded to 1,000 L h^{-1}.

The catalyst, *ca.* 0.6 g, has been suspended in demineralized and outgassed water (*ca.* 1.2 L). Catalyst concentration was chosen in accordance with our previous studies [33,34], in order to avoid diffusional limitation and scattering related to an excessive solid amount. The suspension has been saturated with CO_2 at 7 bar pressure overnight before starting irradiation. The pH was neutral, unless specified differently. Testing was carried out over 24 h continuous irradiation at 7 bar pressure and 80°C (conditions previously optimized [33,34]). The temperature was controlled thanks to a thermosetting bath with circulating fluid and showed approximately the same under dark conditions.

Na_2SO_3 (*ca.* 0.85 g L^{-1}) has been used as hole scavenger and its consumption at the end of the reaction (24 h) was evaluated by standard iodometric titration. Sulphite conversion ranged from 78 to 94% depending on the test. Negligible productivity both in liquid and gas phase has been observed without sulphite addition. We have underlined in a previous work that the hole scavenger allows the accumulation of organic products in liquid phase, whereas after its complete consumption gas phase products (CO and H_2) start forming by photoreforming of the formed organic species [34].

After the reaction, the liquid mixture has been analysed by means of a HPLC (Agilent 1220 Infinity, with a column Alltech OA-10308, 300 mm_7.8 mm), equipped with both UV and refractive index

(Agilent 1260 Infinity) detectors. Aqueous H_3PO_4 solution (0.1 wt%) was used as the eluent. This analysis allowed to quantify HCOOH, HCHO and CH_3OH. HCHO was also quantified in parallel by UV-Vis spectrophotometry through the Nash reactant procedure. The gas phase accumulated in the headspace of the photoreactor has been analysed by a gas chromatograph (Agilent 7890) equipped with HP Plot Q and MS columns and a TCD detector. The set up was proper for the quantification of H_2, CH_4 and polar/non polar light gases. Samplings of 20 cm^3 of gas were collected through a gas syringe and injected in the sampling loop of the gaschromatograph.

Appropriate blank tests have been carried out to ensure the absence of any significant productivity i) in dark conditions, ii) in absence of the catalyst, iii) in absence of the hole scavenger. A specific blank test in absence of CO_2 will be extensively discussed in the following to demonstrate the productivity of organic species by CO_2 rather than from possible organic species contaminating the catalyst or the reaction environment, as often criticized. The same pressure of 7 bar was set with N_2 instead of CO_2 after careful outgassing, the other reaction conditions as for catalyst, hole scavenger, pH and irradiation were the same.

3 - Results and Discussion

3.1 – Morphological, structural and textural characterisation of Au/TiO_2 photocatalysts

Au catalysts have been prepared by deposition precipitation method with urea and using $NaBH_4$ as reducing agent [40] using TiO_2 as support (P25, rutile and anatase). For P25, Au/TiO_2 samples with different loading (0.1, 0.2, 0.5 wt%) have been prepared, whereas for rutile and anatase 0.5 wt% Au loading has been considered, only. Figure 1 shows the different polymorphs of TiO_2 in the 0.5 wt% Au samples. Au reflections have been never observed due to the very low Au loading and the small gold nanoparticle size. 0.5 wt% Au/rutile was predominantly composed by rutile (96% rutile, 4% Anatase), 0.5 wt% Au/Anatase by Anatase (97% Anatase, 3% Rutile) and 0.5 wt% Au/P25 by a mixture of Anatase (78%) and Rutile (22%). Crystallite size was calculated from XRD using the Scherrer equation. P25 TiO_2 was characterized by small crystal size (~15 nm), much smaller than

Rutile (~83 nm) and Anatase (~92 nm). These results are in good agreement with the values previously reported for 0.1 wt% Au/TiO_2 [33].

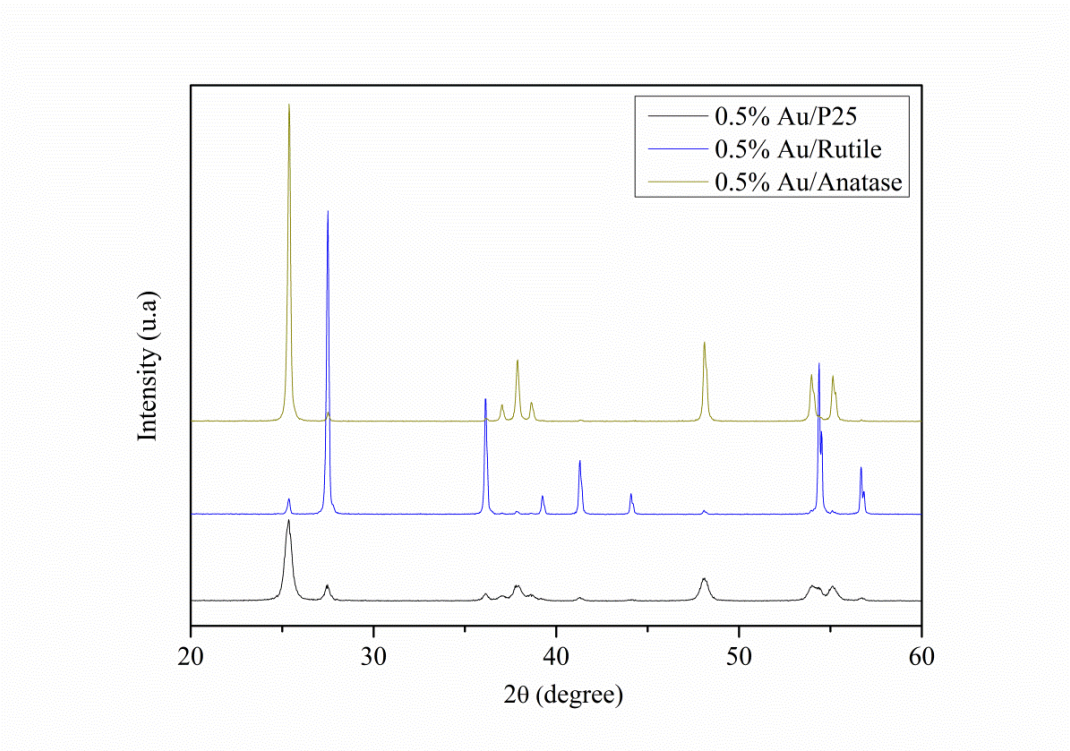

Fig. 1: XRD patterns of different 0.5 wt% Au/TiO_2 catalysts. From bottom up, P25, rutile and anatase.

STEM images of Au/TiO_2 catalysts showed well-dispersed metal nanoparticles on TiO_2. In Figure 2 we reported representative images of 0.5 wt% Au/P25, 0.5 wt% Au/Anatase and 0.5 wt% Au/Rutile. Au particle size was determined from STEM and HRTEM images (Figures 2 and 3) and the results are summarized in Table 1).

All the catalysts revealed small Au particle size, in the range of 3.7-4.7 nm. Comparing the Au/P25 samples, an increase of the particle diameter by increasing the Au loading was observed: 3.7 nm, 4.0 nm, 4.6 nm, for 0.1 wt% Au/P25, 0.2 wt% Au/P25, 0.5 wt% Au/P25, respectively, Table 1. By contrast, similar Au particle size was obtained when depositing 0.5 wt% Au on P25 and Rutile (4.6 and 4.7 nm, respectively), whereas on Anatase Au particle diameter was lower (3.8 nm) (Table 1).

The labelling of *d* spacings are reported for different TiO_2 supports and for Au. In the case of rutile support, the particle was very big and the crystallinity so poor that the lattice of rutile structure is not clearly visible. For P25, both rutile and anatase were detected.

Table 1. Statistical Median of Particle Size obtained by HRTEM, Specific Surface Area (SSA), XRD

Sample	Statistical Median (nm)	Standard Deviation (nm)	SSA (m^2/g)	XRD (TiO_2)
0.1 wt% Au/P25	3.7	0.9	52	78% anatase 22% rutile, 15 nm
0.2 wt% Au/P25	4.0	1.0	55	78% anatase 22% rutile, 15 nm
0.5 wt% Au/P25	4.6	1.6	50	78% anatase 22% rutile, 15 nm
0.5 wt% Au/Anatase	3.8	1.3	8	97% anatase 3% rutile, 92 nm
0.5 wt% Au/Rutile	4.7	2.4	1	96% rutile, 4% anatase, 83 nm

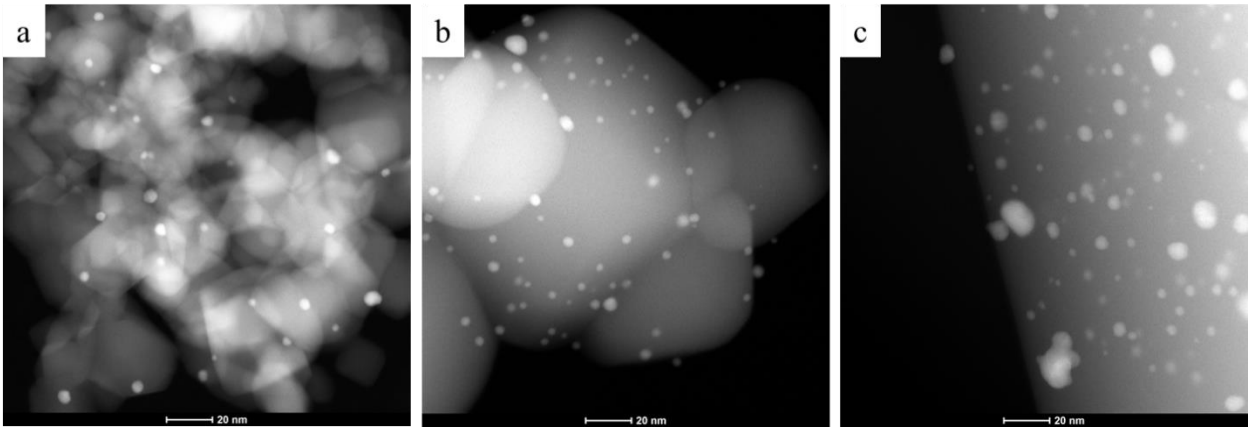

Fig. 2: Representative STEM images of 0.5 wt% Au loaded on a) P25, b) anatase and c) rutile TiO_2. Marker size 20 nm

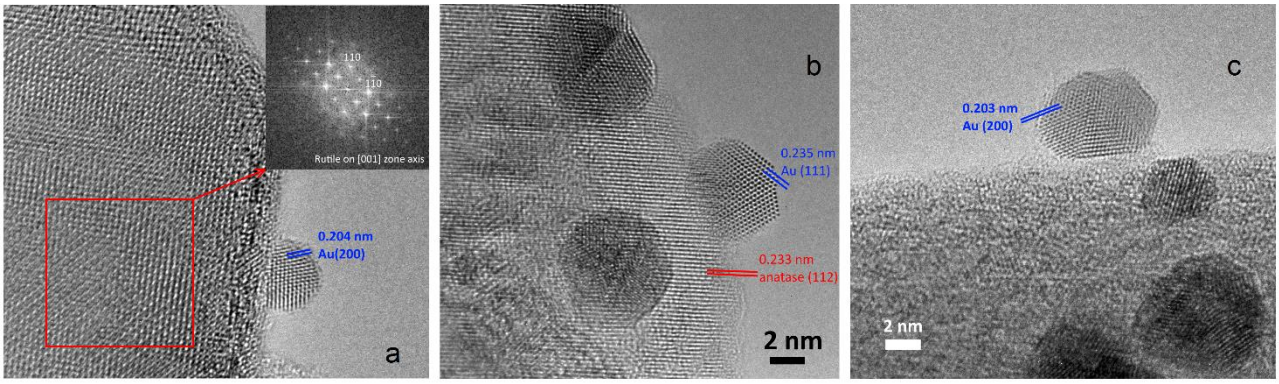

Fig. 3: Representative HRTEM images of 0.5 wt% Au loaded on a) P25, b) anatase and c) rutile TiO_2. Marker size 2 nm.

3.2 – XPS and DRIFTS

The charge of gold plays an important role in the process, affecting the charge trapping efficiency, migration, recombination and interfacial charge transfer [41]. The oxidation state of gold has been studied by XPS, which confirmed the surface composition of the samples and the presence of metallic Au both in the fresh and the spent catalysts [32]. CO-DRIFTS adsorption analyses were also carried out to further elucidate this point (Figure 4). This technique is very powerful for the detection of metal dispersion and oxidation state [42,43]. For all the Au/P25 fresh samples the adsorption of CO gave rise to one or two IR bands in the CO carbonyl spectral region (1950–2150 cm^{-1}). The highest frequency IR band (2106 cm^{-1}) was attributed to linearly adsorbed CO on metallic gold and it strictly dependent on gold nanoparticles diameter. Therefore, with increasing the wt% of Au loading on P25, the intensity of this peak increased (Figure 4) [44]. The broad and asymmetric band at lower frequencies with the maximum located at 2040-2072 cm^{-1} was attributed to the linearly, multisite and bridged CO on $Au^{\delta-}$ [44]. The observation of this band is mainly due to the electron transfer from reducible titania support to small gold nanoparticles or clusters [44].

The intensity of both bands increased with Au loading. Anatase and, most of all, rutile materials revealed a markedly higher amount of partially negative gold particles, with respect to 0.5 wt% Au/TiO_2 P25, for which the intensity of the two bands was similar. This could be correlated with the larger titania crystal size characterizing the rutile and anatase samples, as detected in XRD analysis.

Furthermore, XPS analysis is in line with these data. At first it confirms partially negative charge on Au particles (binding energy ca. 82.9 eV for the present samples with respect to standard values of 84 eV for Au^0). Furthermore, Fig. 5 evidences a lower surface exposure of Au (per unit surface) for 0.5 wt% Au/TiO_2 P25 with respect to the other two TiO_2 samples. This again agrees with the higher amount of negatively charged Au detected by CO-DRIFS analysis.

CO_2 adsorption on P25 gives rise to several IR bands in the range of 1800-1000 cm^{-1} [32]. Three main peaks at 1312, 1416 and 1577 cm^{-1}, with a shoulder at higher frequency, respectively assigned to CO_2

bent, bicarbonate HCO_3^- and bidentate carbonate (b-CO_3^{2-}) species were detected. The nature of carbonate form present is related with to titania crystalline form. The role of water has been studied performing experiment under dry and wet conditions. In presence of water vapour, a marked increase of the relative intensity of band 1312 and 1675 cm^{-1} was detected (*i.e.* peak height subtracted by the baseline of the spectra) suggesting that H_2O promotes the formation of the CO_2 radical anion, with a synergistic effect for CO_2 photoreduction. For the gold sample, a further band at 1199 cm^{-1}, associated with a particular bicarbonate, was present. Moreover, also the greater surface area of P25 with respect anatase and rutile should be considered. In fact, over P25, Au particles are more dispersed and isolated so promoting the linear adsorption of CO over the small gold particles. On the contrary, over the other samples, with a lower surface area, the gold nanoparticles are less dispersed favouring the formation of bridged CO adsorbed species.

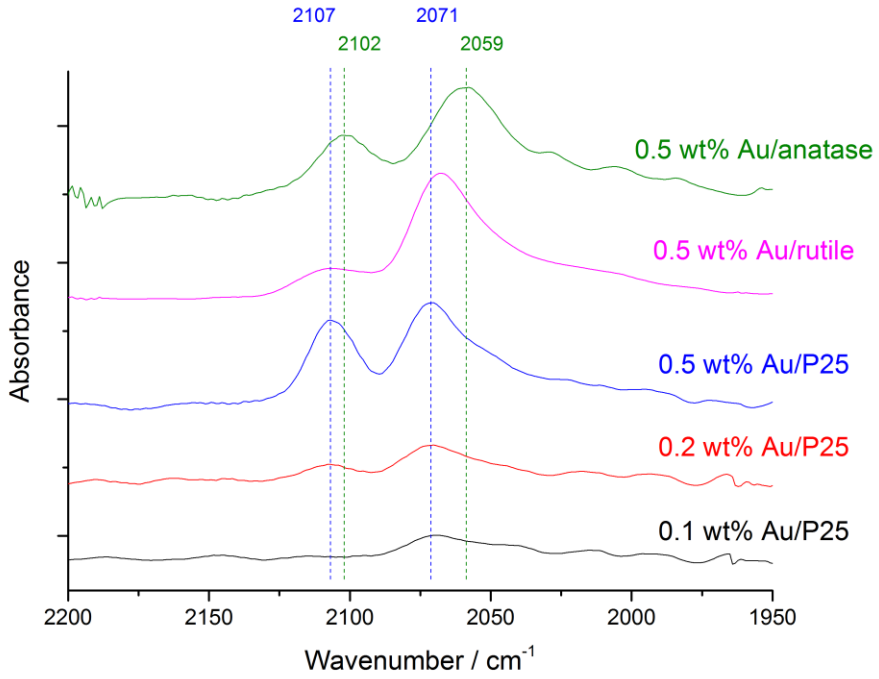

Fig. 4: DRIFTS spectra of the fresh samples using CO as probe molecule.

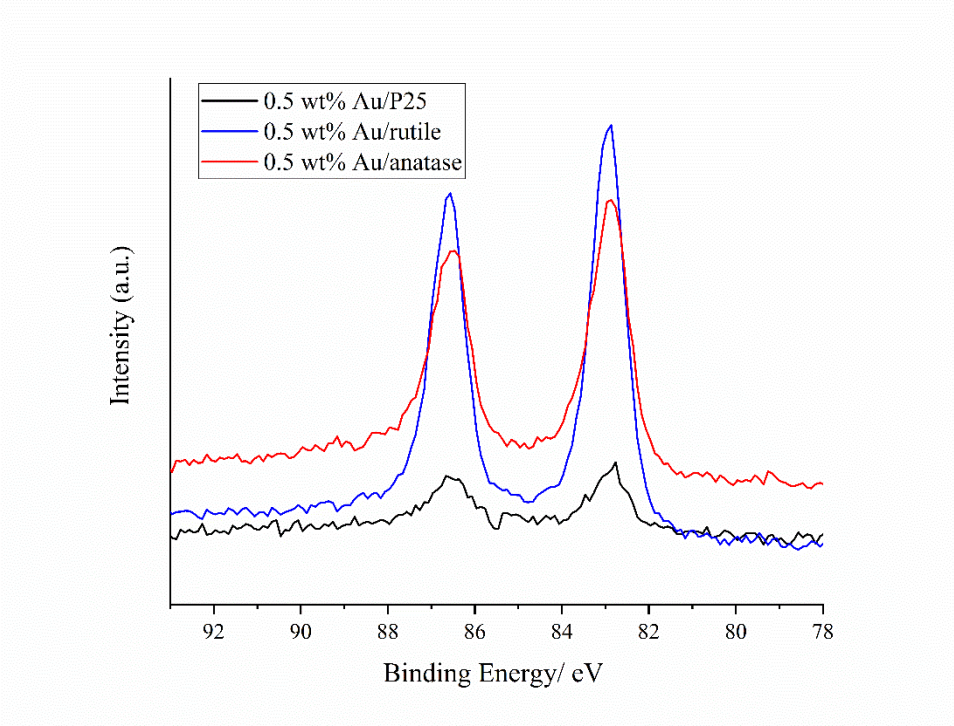

Fig. 5: XPS spectra of the fresh samples with 0.5 wt% Au over different TiO_2.

3.3 - Structure-activity correlation for CO_2 photo-reduction

Preliminary blank tests were carried out to enhance the effect of:

i) Irradiation. A test in dark conditions allowed to exclude non photoinduced effects, since the productivity was below the detection limits for all the products.

ii) Photocatalyst. A blank test without the photocatalyst, under irradiation, returned negligible productivity for all products.

iii) Hole scavenger. Insignificant amount of products (3 orders of magnitude lower productivities) was observed in the absence of the hole scavenger.

iv) Possible organic impurities. In order to compare the reactivity towards hydrogen production through direct water splitting and CO_2 photoreduction, a test at 7 bar of nitrogen was compared with the ones in CO_2 atmosphere. In presence of nitrogen the main use of the photo-generated electrons in the CB, besides recombination, is the reduction of

H^+ to H_2. The test with nitrogen confirmed this result, with an unexpectedly high productivity of *ca*. 350 mmol H_2 kg_{cat}^{-1} h^{-1} at 7 bar pressure, but nil productivity to HCOOH, HCHO and CH_3OH by using the 0.1 wt% Au/TiO_2 catalyst. H_2 production comes from the water splitting, aided by the addition of the inorganic hole scavenger and is, as it will be evident in the following, much more effective than in the presence of CO_2 due to competitive reaction of the promoted electron for the reduction of H^+ and CO_2 when the latter is present. This test definitely demonstrates that the organic products are due to the photoreduction of CO_2 and have no correlation with possible organic impurities present on the catalyst (*e.g*. organic residua from the preparation) or in the apparatus.

The possible reaction paths are depicted in Fig. 6.

3.3.1 - Effect of the gold-loading

Temperature, pressure and pH are very critical parameters for the CO_2 photo-reduction processes [1]. A comprehensive study of the high pressure CO_2 photo-conversion was carried out in one of our previous papers in order to shed light on the complex reaction pathways towards both liquid and gas phase photo-reduction products [34]. In such case, TiO_2-P25 was chosen as reference material and products distribution was compared at different reaction time and pH conditions. The formation of formaldehyde was independent from that of formic acid and constituted the major product during tests at shorter reaction time (3-16 h). By contrast, at longer reaction time (24-72 h) only gas-phase products were present (H_2 and CO) due to the consecutive step of photo-reforming (Figure 7).

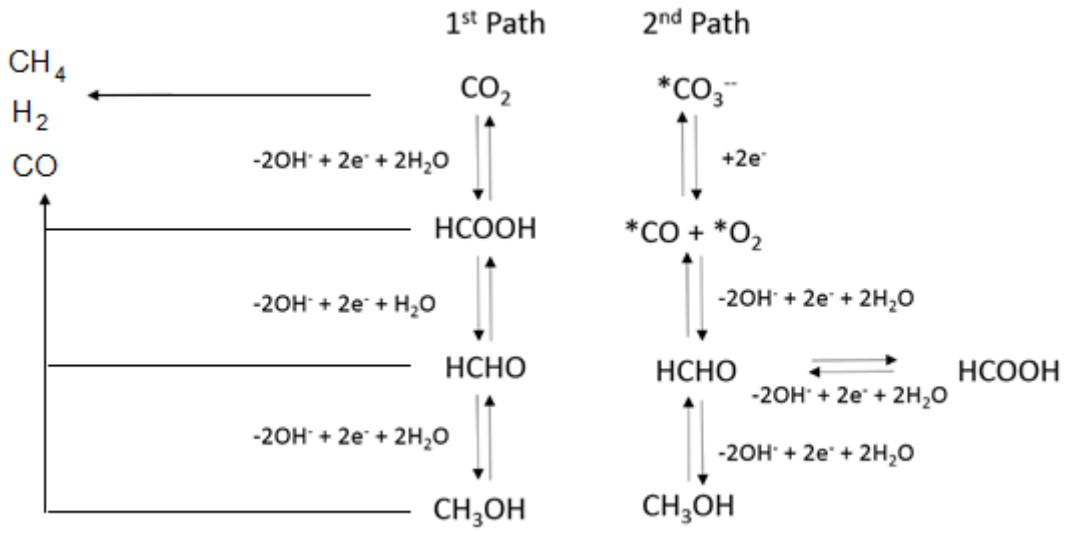

Fig. 6: Scheme of the two possible paths for molecular CO_2 and carbonate photoreduction. The symbol * indicates the species adsorbed on the photocatalyst surface. The same routes to gas phase products (CH_4, H_2 and CO) hold also for the 2nd path.

No methanol or methane were detected in the case of bare TiO_2. Two parallel reaction pathways were observed. The first one involved the photoreduction of molecular carbon dioxide to formic acid, which may reduce further to formaldehyde and methanol in a strictly consecutive path or evolve to gas phase products by photoreforming, *i.e.* the formation of H_2 + CO/CO_2 by oxidation of the accumulated organic molecules (HCOOH, HCHO, CH_3OH) through the photogenerated holes. This latter route has been already demonstrated by us [30] observing the H_2/CO formation only after all the sulphite HS has been consumed, with a simultaneous decrease of the organics concentration in the liquid phase. The latter reaction occurs only when the hole scavenger is fully consumed, so that the valence band holes oxidise the organic species accumulated in the liquid phase, while conduction band electrons are used to reduce protons to molecular hydrogen. The second mechanism implies the reduction of carbonates to give formaldehyde and possibly methanol in a further consecutive step. Also in this case photoreforming, leading to the production of H_2 and CO at the expenses of the

organic products accumulated in the liquid, is a consecutive step after consumption of the hole scavenger. The results led to the conclusion that at basic pH (12-14) the mechanism is tightly related with the conversion of CO_2 in carbonate while at neutral pH two hypothesis can be formulated: a) the mechanism is the 2nd one, but running at a lower rate (low carbonate concentration); b) the first path is preferred.

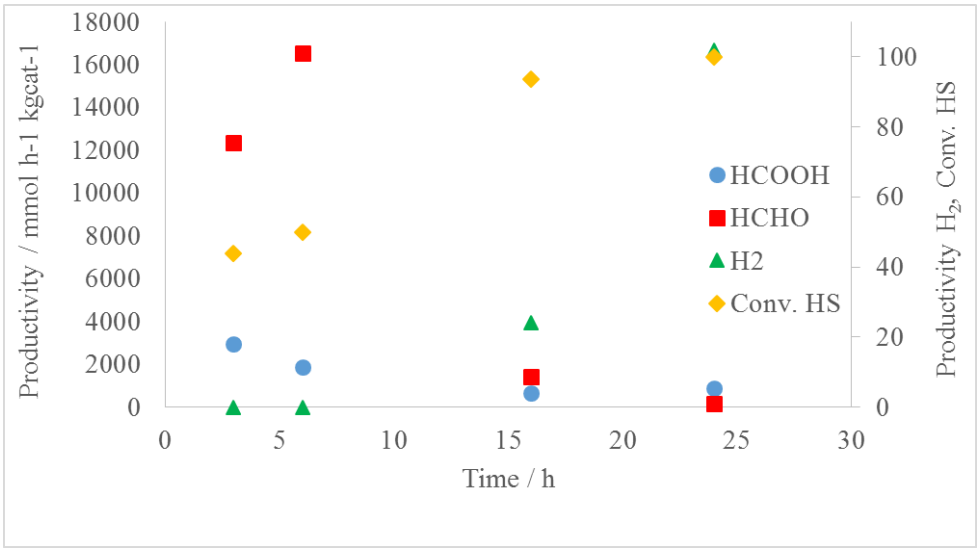

Fig. 7: Evolution of the various products *vs.* reaction time for TiO_2 P25 at 7 bar, 80°C. Productivity expressed as mmol kg_{cat}^{-1} h^{-1} for HCOOH and HCHO (left axis) and for H_2 (right axis). The conversion (%) of the hole scavenger (Na_2SO_3) is also reported (right axis) [34].

The addition of a metal to TiO_2 decreases the band gap of this material and improves visible light absorption and the lifetime of the photogenerated charges. For instance, the comparison of the DR-UV spectra of a sample of TiO_2 P25 and a 0.2 wt% Au loaded sample revealed that the absorbance curve for the Au containing sample was shifted towards larger wavelengths and the corresponding Tauc plot resulted in a band gap calculation decreasing from 3.36 to 3.17 eV after gold loading [45]. Furthermore, Au addition modifies the potential of electrons [33,34], thus possibly modifying the

products distribution. Based on our previous work [33,45] the use of various TiO_2 polymorphs and Au addition effectively tuned the band gap of this material from 3.36 eV (bare P25 TiO_2) to 3.08, 3.24 and 3.02 eV for Au/P25, Au/Anatase and Au/Rutile respectively.

Testing was here carried out at neutral pH, which is more interesting from an applicative point of view. The results of activity testing at 7 bar, 80°C, 24 h reaction time, with Au/TiO_2 P25 at variable metal loading are reported in Figure 8.

Methanol was the main product in liquid phase, demonstrating the higher reactivity of the present Au-loaded samples with respect to the bare semiconductor. It should be also interestingly noticed that methanol is not formed after 24 h at pH=14. By looking to the relative products amounts, the intermediate concentration of formaldehyde confirms the validity of the reaction scheme proposed in [34]. The highest methanol productivity was achieved with Au loading 0.2 with a slightly higher yield of the less desirable products (formic acid and formaldehyde).

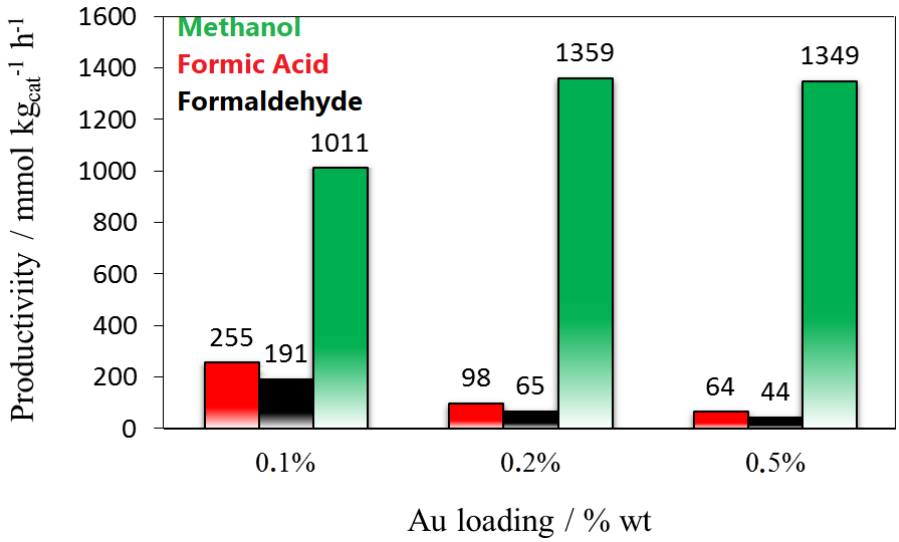

Fig. 8: Liquid phase productivities at variable Au loading (T=80°C, p=7bar, pH=7)

An approximate comparison of the present methanol productivity with respect to literature data is reported in the following Table 2. Of course, this comparison cannot take into account the reactor configuration, the distribution of the radiation and of the suspended particles, issues very important,

but difficult to evaluate if there are not specific fluid dynamic models of the photo-reactor used. Nevertheless, the high methanol productivity achieved with the present Au-doped catalysts under high CO_2 pressure is well evident.

Table 2: Comparison of the present Au/TiO_2 catalysts for CO_2 photoreduction with state of the art results.

Catalyst	**UV power lamp**	**UV wavelength (nm)**	**Methanol productivity (mmol kg_{cat}^{-1} h^{-1})**	**Reference**
0.5 wt% Au/TiO_2	77 W m^{-2}	254-365	1350	This work
0.5% Au/TiO_2	71.7 W m^{-2}	365	0.5	[46]
1% Cu-3% In_2O_3/TiO_2	250 W m^{-2}	365	35	[47]
3% CuO/TiO_2	24.5 W m^{-2}		442	[37]
Cu/TiO_2	8 W	254	20	[48]
Ti-β zeolite	-	254-365	680	[2]
Ti-SBA-15	100	>250	27.7	[49]
Cu/TiO_2/MS	250 W	365	2	[50]
NiO	960 W m^{-2}	340	393	[51]
o-$BiVO_4$ layers	1000 Wm^{-2} (300 W Xe lamp)	350, 380, 400, 450, 500, 550, 600, and 650	398.3	[52]
Zn_2GeO_4 nanorods	500 W Xe lamp	> 400	0.143	[38]
Bi_2S_3-TiO_2	500 Xe lamp	> 400	65	[44]

The samples showed promising activity also for the formation of high valued gas phase products, *i.e.* H_2, CO and methane. Methane is produced by direct photoreduction of CO_2. It was never observed for bare titania photocatalysts, whereas Au doping allowed its formation. The productivity of methane increased abruptly when doubling the Au amount from 0.1 to 0.2 wt%, then very slightly when passing to 0.5 wt%. This can be correlated to the increasing surface concentration of Au nanoparticles and confirms the role of the surface area of the exposed Au nanoparticles on this reaction pathway.

As for CO, it can be either obtained by *i)* direct photoreduction, or *ii)* as a product of photoreforming of the organic compounds obtained in liquid phase by CO_2 photoreduction, or *iii)* by decomposition of HCOOH, or even *iv)* by catalytic reduction of CO_2 by using the photogenerated H_2. The productivity trend of CO and H_2 are well visible in Figure 9 and are very similar. This suggests that both species are produced by photoreforming of the primary organic products of photoreduction accumulated in the liquid phase.

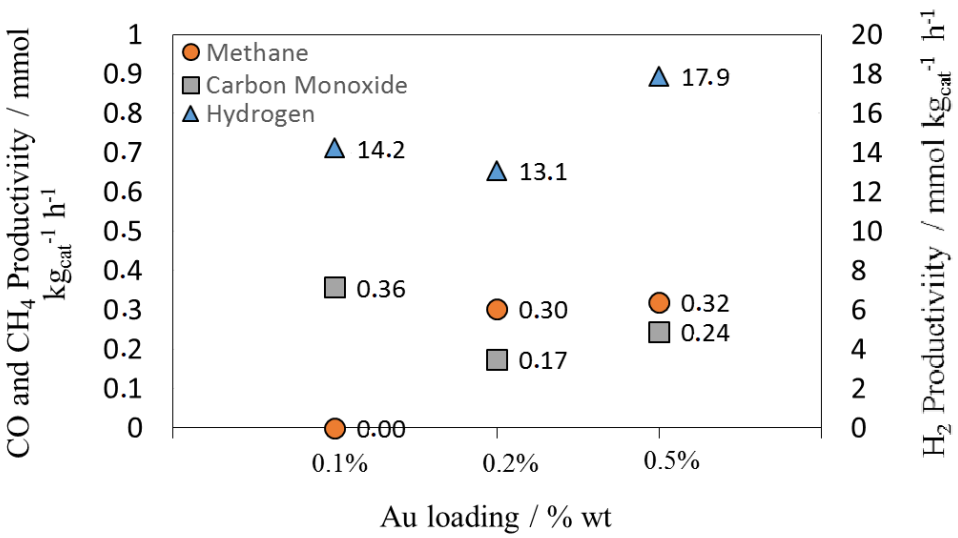

Fig. 9: Gas phase productivities varying the Au loading (T=80°C, p=7bar, pH=7)

A methane productivity of 0.30 and 0.32 mmol kg_{cat}^{-1} h^{-1} was obtained for 0.2 and 0.5% Au/TiO_2-P25 respectively. By contrast, no traces were detected in gas effluents after tests using bare P25 and

0.1 wt% Au/TiO_2-P25. This critical point deserves further discussion due to the implications associated.

Collado et al. performed several CO_2-photoreduction tests using a gas-phase configuration and gold/titania catalysts prepared by DP method using NaOH [46]. The highest CH_4 production was obtained with 1.0 wt% Au/TiO_2-anatase sample with a maximum productivity of *ca*. 8.9 mmol kg_{cat}^{-1} h^{-1}, using UV light (365 nm) and an average intensity of 71.7 W m^{-2}, similar to the present conditions. Hydrogen productivity was maximum 9.5 mmol $kgcat^{-1}$ h^{-1}, and was attributed to the competitive reaction of H_2O reduction by photo-generated electrons. Although only the anatase crystalline form was investigated, a stronger enhancement of carbon monoxide productivity was obtained decreasing the metal loading, combined with a decrease of methane selectivity.

Matejová and co-workers studied several gold-oxide photocatalysts, obtaining a maximum hydrogen and methane productivity at 160 and 6 mmol kg_{cat}^{-1} h^{-1} respectively [53], but no liquid phase products were reported.

In our case at 7 bar, the highest loading of Au revealed the highest methane and hydrogen productivities. Thus, it can be considered the most promising among this series, although leading to a slightly lower formation of methanol (1350 mmol h^{-1} kg_{cat}^{-1}) with respect to sample 0.2 wt% Au (1360 mmol h^{-1} kg_{cat}^{-1}).

The good performance of very low gold loading on titania was confirmed recently by Tahir et al. [54]. In particular, they investigated the incorporation of gold nanoparticles at low loading within TiO_2 nanowires as suitable materials for the CO_2 photoreduction in gas-phase under visible light. The optimum loading of Au for methane productivity was obtained using the 0.5 wt%, however the analogues 0.2 wt% and 0.7 wt% revealed lower activity.

3.4.2 - Effect of the titania polymorph phase

The crystal phase of the titania photocatalyst was varied as well. This aspect is important because many publications discuss the effect of titania polymorphs in the oxidative photocatalytic applications, but only few of them are related with reductive photocatalysis. The highest metal loading was chosen (0.5 wt%) for all the samples because of the slightly enhanced total productivity and due to the much stronger plasmonic band associated. For this reason, this material is very interesting also for the next process implementation using visible radiation under high pressure, because of the higher visible light harvesting.

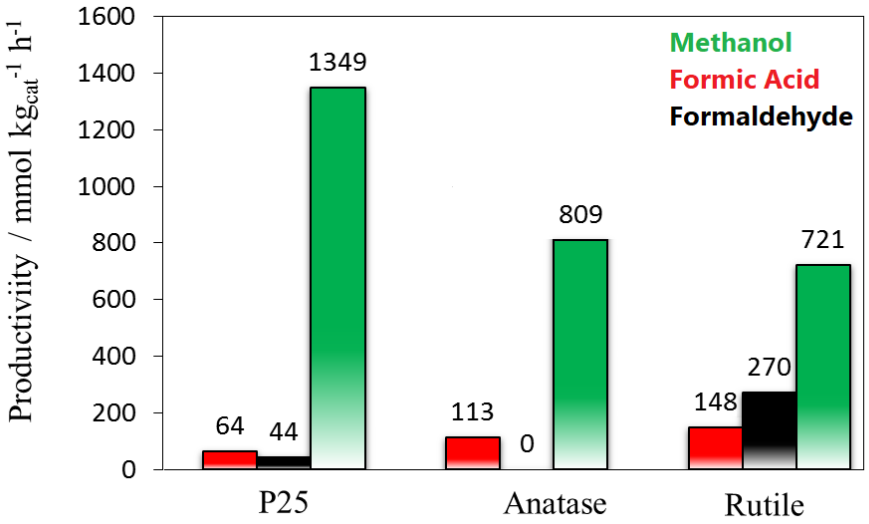

Fig. 10: Liquid phase productivities with different titania crystalline phase (T=80°C, p=7bar, pH=7)

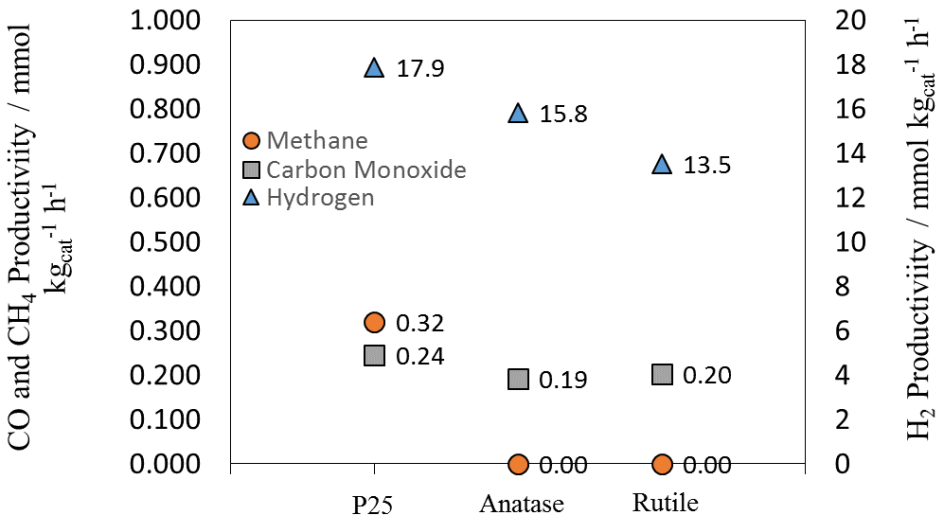

Fig. 11: Gas phase productivities varying the titania crystalline phase.

In particular, the commercial Evonik P25 titania was used as mixed titania phase, while pure anatase and rutile as single titania phase supports.

Methanol productivity (Fig. 10) was very high for all the samples and promising with respect to the most representative papers reported in literature (Table 2). Much higher methanol productivity was achieved for the P25-based sample, at the expenses of the more oxidized intermediates. On the other hand, the complete absence of formaldehyde for the anatase-based sample and its highest productivity for the rutile base sample suggests the promotion of the carbonate-based reaction path by rutile. This hypothesis is supported by the low productivity of formaldehyde of P25, which is a mixture 78:22 of anatase and rutile. These results support the validity of the approach to fix CO_2 through a contemporary storage of solar energy [36].

Methane was obtained only for the mixed phase P25 sample. The direct photoreduction of CO_2 to methane is indeed a complex multielectronic pathway. The greatest activity usually exhibited by the titania P25 mixed phase is ascribed to the electron transfer from one phase to the other, which acts as

electron sink, thus inhibiting the electron-hole recombination. Therefore, only by increasing the lifetime of the photogenerated electron the direct CO_2 photoreduction can safely proceed to methane.

Also, the photocatalytic activity towards H_2 and CO production was higher in the case of the P25 mixed phase than for the pure anatase and rutile phases. As highlighted before, their productivity trend was similar, confirming their origin from the photoreforming of organic compounds rather than by direct reduction.

Delavari et al. explored the gas phase reaction using immobilized TiO_2 nanoparticles on a stainless steel mesh [55]. Considering the crystalline phase, an increase of CO_2 and CH_4 conversions were detected due to the increase of the anatase/rutile ratio in TiO_2, in such a case directly correlated with the enhancement of surface area. Mixed-phase titania nanomaterials were studied by Chen et al., for gas phase CO_2 photoreduction involving the DC magneton sputtering as preparation method [56]. All the mixed-phase sputtered samples displayed greater extent of reaction compared to single phase ones. The results were correlated to the high density of interfacial sites.

The synergistic effect between rutile and anatase for photo-catalytic applications is not new in the literature, but the deep explanation of the phenomena is still under debate [15]. The more consistent argumentation considers the low electron-hole recombination as consequence of the spatial separation caused by the interconnection between rutile and anatase particles. Li et al. investigated several TiO_2 polymorphs as a photo-catalyst for CO_2 reduction under UV light illumination [57]. They found a very different methane production varying the crystalline phase of the titania. The synergistic effect was apparently demonstrated because higher photocatalytic activity was obtained using a mixed-phase TiO_2. On the contrary, Ohtani et al. supported a contrasting explanation, considering the lack of information about the direct evidence of the inter-particle charge migrations and the expected lower level of activity of pure anatase or rutile particles alone [15]. For this reason in another work [58] they prepared a reconstructed P25 (mixture of pure anatase, rutile and amorphous titania) and demonstrated a less probable synergistic effect for the oxidative decomposition of acetic acid,

acetaldehyde and methanol dehydrogenation. Recently Kafizas et al. [59] employed transient absorption spectroscopy to study the hole transfer process across the anatase-rutile heterojunction in films as a function of phase composition, revealing a real difference between the electron hole recombination time using different titania forms. In addition Kullgren et al. [60] investigated the phenomena by photoelectron spectroscopy and flat-band potential measurements in the case of mixed-phase nanoparticles in humid environment. Although the explanation is still far from an unmistakable solution, the higher activity of mixed rutile-anatase TiO_2 was still reported for CO_2 photo-reduction in literature, and our results confirmed this trend also for the present unconventional high pressure conditions.

Similar CO productivity rates were obtained for all the samples, ascribable to two main reasons: i) the CO formation occurred through a reaction independent and without any contribution of the photo-catalyst, such as the CO_2 photolysis; ii) the CO formation occurred independently from the metal loading; iii) photoreforming. The directly photolysis of CO_2 is the less probable option in our conditions. The CO_2 splitting occurs in the so called deep UV region (wavelengths below 200 nm requiring pure quartz or metal halides and vacuum):

$CO_2 + hv\ (<200nm) \rightarrow CO + 1/2\ O_2$ $(\Delta H = +257\ kJ\ mol^{-1})$ [7]

The blank test without the catalyst revealed negligible CO productivity and ruled out definitely the first hypothesis. The independence on metal loading in the studied range can be explained considering a detailed work of Lin et al. [61]. A direct correlation between Ti centers and CO_2 reduction to CO by water in presence of the UV irradiation was obtained using mesoporous framework substituted Ti silicalites. The proposed mechanism involved the formation of a transient Ti^{3+} and a hole on a framework oxygen (Ti^{+3}-O^{-}) after the excitation of the Ti centers (Ti^{4+}-O^{2-}). Therefore, the effective role of Au, as electron sink is not useful in this context.

The hydroxylation of the surface, examining the characteristic Ti–OH bonds, changing the support was carried out in order to investigate this feature often correlated with the photo-activity of the

catalysts [62]. Indeed, hydroxyl groups have been recognized to play an important role in the photo-catalytic processes through their interactions with photo-generated holes [63,64] and the preparation method directly affects the hydroxylation state of the catalyst surface. The experimental DRIFTS spectra reported also in the present case the different OH species depending on the titania used (Figure 12). Generally, hydroxyl groups can be divided in two main types considering the TiO_2 surface: isolated hydroxyls (3600-3700 cm^{-1}) and H-bonded hydroxyls (3400-3450 cm^{-1}) [63–65]. The band at 3691 cm^{-1} relative to the stretching vibration of H-bound OH group was present for all the samples but in different intensity [64]. P25 revealed also a peak at 3629 cm^{-1} corresponding to physically adsorbed H_2O [66] while rutile a peak at 3410 cm^{-1} often ascribed to symmetric and antisymmetric OH modes of molecular water coordinated to Ti^{4+} cations [66]. All these hydroxyl species are more intense in the case of P25, whilst decrease going to anatase and rutile. Although no significant correlation can be found considering the liquid-phase product obtained by the photoreduction process, the results are in line with the hydrogen productivity, as reported in Figure 13. This is in accordance with Maira et al. that reported the correlation between isolated hydroxyl groups and adsorption/photooxidation activity [64].

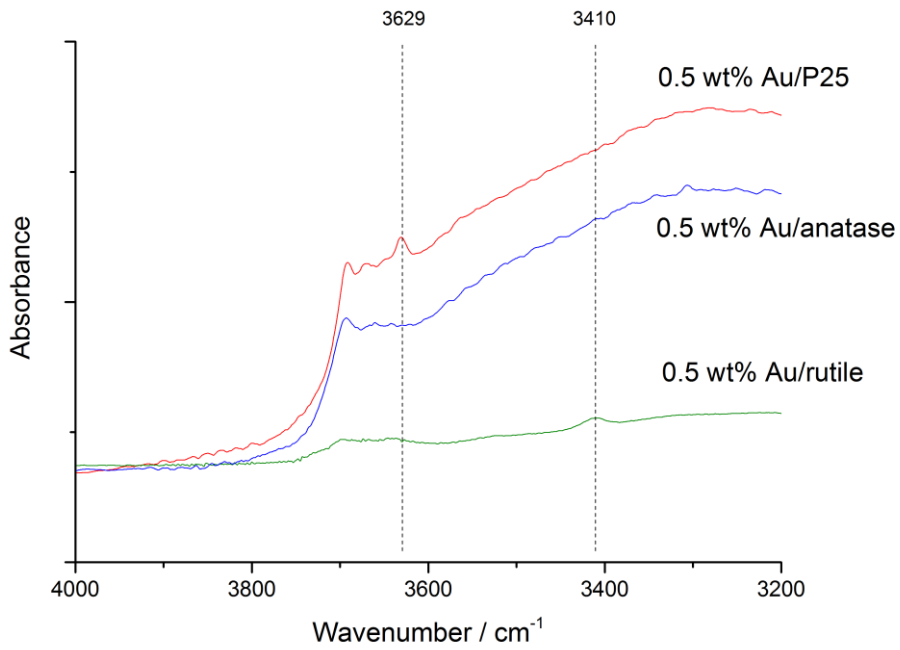

Fig. 12: DRIFTS spectra of OH groups in the region of 3200−4000 cm^{-1} for the different titania samples.

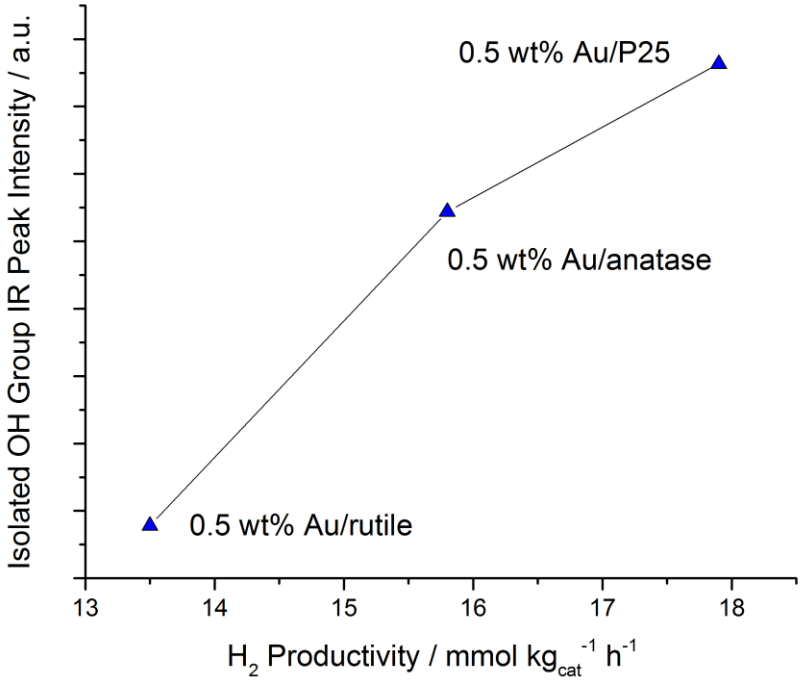

Fig. 13: H_2 productivity versus OH peak intensities for the different titania samples.

In order to compare the reactivity towards hydrogen production through direct water splitting and CO_2 photoreduction, a test at 7 bar of nitrogen was compared with the ones in CO_2 atmosphere. In presence of nitrogen the main use of the photo-generated electrons in the CB, besides recombination, is the reduction of H^+ to H_2. The test with nitrogen confirmed this result, with an unexpectedly high productivity of *ca*. 350 mmol H_2 kg_{cat}^{-1} h^{-1} with respect to the 17.9 mmol H_2 kg_{cat}^{-1} h^{-1} obtained under CO_2 atmosphere. The fundamental role of the photocatalyst was finally confirmed by the blank test without any catalyst, where no hydrogen was detected.

Mechanistic details associated with single electron transfer events are few. CO^{-}_2 is believed by some groups to be a key surface intermediate in photoreduction on TiO_2, implying direct electron attachment to an adsorbed CO_2-containing species [12]. The transition from this species to those

possessing C–H bonds is still unclear. We interpret this raise in productivity of all the reduced organic products with respect to literature as due to the increase of CO_2 pressure. This leads to an increase of the dissolved CO_2 fraction (even if operating at high temperature, as predicted by thermodynamics and extensively described in [27]). Indeed, operating at 80°C, the CO_2 molar fraction at saturation is calculated as *ca*. 0.01at 1 bar, *ca*. 10% at 7 bar and *ca*. 35% at 20 bar. This in turn increases the amount of reactant adsorbed on catalyst surface, overcoming one of the limits of this reaction in liquid phase.

Also, the increase of adsorbed CO_2 can influence the reaction rate of the different consecutive and parallel steps of Figure 6, thus leading to a different products distribution. At higher pressure the formation of products in liquid phase is favored over the consecutive photoreforming path to H_2 (Figure 14). Depending on pH HCOOH was favored or not over methanol, which is the final consecutive reaction product. Indeed, the abundant CO_2 consumes the available electrons through the first reaction step. When the amount of dissolved and adsorbed CO_2 is lower, the further reduction of the intermediates (HCHO and CH_3OH) is instead favored. The pH can also strongly influence the products distribution, as already discussed elsewhere, neutral pH favoring the consecutive path to methanol with respect to the accumulation of HCOOH, which is the main product at pH=14. Thus, we compared the effect of pressure at this latter pH in order to simplify the products distribution and have an overall check on the reaction pathways (Figure 14). From this comparison it is clearly seen that an increase of pressure favors the accumulation of HCOOH at the expenses of the consecutive photoreforming path.

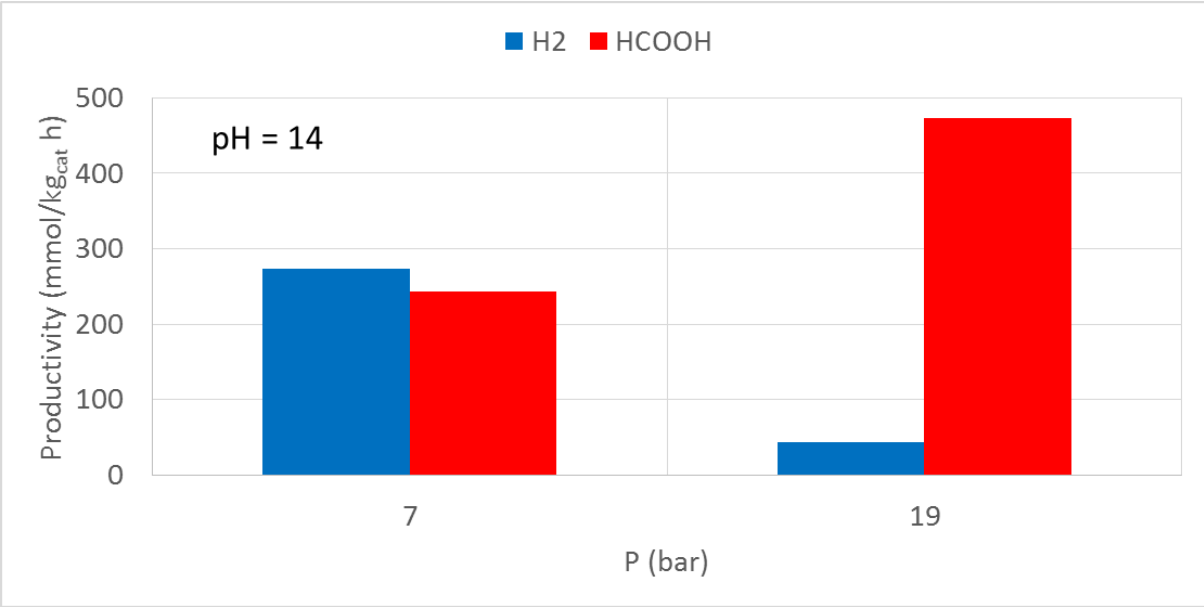

Fig. 14: H_2 and HCOOH productivities varying the pressure; Sample 0.2wt% Au/P25 at T=80°C and pH = 14.

The apparent quantum yield (AQY) has been here calculated as follows:

$$AQY\ (\%) = \frac{\text{moles of product(i)}\ per\ second\ \times\ \nu(i)}{Incident\ photons\ per\ second}$$

ν(i) is the number of electrons consumed to reduce CO_2 to the desired product (*e.g.* 6 for methanol) and is directly calculated from the productivity data here reported.

The incident photons flow has been calculated based on the measured intensity of radiation (as reported in the experimental) multiplied by the receiving surface. In this case we have considered an average cylindrical surface surrounding the lamp and coaxial with it. It has been approximated considering an average radius between that of the lamp (r_{lamp}) and of the reactor ($r_{reactor}$). Due to the cylindrical symmetry a logarithmic mean has been considered most suitable. The energy of each electron has been calculated from the speed of light in water (*ca.* 2.2 10^8 m s^{-1}) with a wavelength of 365 nm).

Considering the highest methanol productivity here reported (1359 $mmol_{CH3OH}$ h^{-1} kg_{cat}^{-1}) we have calculated an AQY = 11.38%.

Conclusions

The photocatalytic reduction of CO_2 in water was studied at high pressure under optimized conditions, investigating the role of Au loading and TiO_2 crystalline phase. In particular, a modified deposition/precipitation method was adopted for the synthesis on 0.1 wt%, 0.2 wt% and 0.5 wt% Au/TiO_2. Commercial P25, pure anatase and pure rutile were used as semiconductors. Methanol productivities of 1359 and 1349 mmol kg_{cat}^{-1} h^{-1} were detected for 0.2 wt% Au/TiO_2 and 0.5 wt% Au/TiO_2, respectively, showing the promising potential use of supported gold catalysts with low Au loading. The highest loaded sample led also to the highest H_2 and CH_4 productivities (17.9 and 0.32 mmol kg_{cat}^{-1} h^{-1}). By contrast, lower activity was achieved using anatase and rutile pure phases, confirming the key role of interfacial defects for enhancing the lifetime of the photo-generated charges between borders of different crystalline phases.

High pressure tests allowed to conclude that increasing the pressure favors the accumulation of organic reduced products in liquid phase, whereas gas phase productivity is favored at intermediate pressure. Au was needed to produce methanol and methane and the former did not form in basic pH conditions.

These processes can be applied for CO_2 conversion while simultaneously converting this greenhouse gas to high valued products such as methane, methanol, formaldehyde or formic acid, especially towards methanol economy. Very high methanol productivity was achieved with the present catalysts, incomparably higher than the better results reported in the literature (*ca.* 1.4 mol kg_{cat}^{-1} h^{-1}).

Conflicts of interest

There are no conflicts of interest to declare.

Acknowledgements

The valuable help of M. Compagnoni, PhD and of the graduating student D. Vitali is gratefully acknowledged.

I. Rossetti and E. Bahadori are grateful to Fondazione Cariplo and Regione Lombardia for financial support through the grant 2016-0858 – Up-Unconventional Photoreactors.

The financial contribution of MIUR through the PRIN2015 grant (20153T4REF) is gratefully acknowledged (G. Ramis and I. Rossetti).

A. Villa and D. Wang are grateful to Karlsruhe Nano Micro Facility (KNMF) long term Project for financing TEM work.

References

1 P. Usubharatana, D. McMartin, A. Veawab, P. Tontiwachwuthikul, F. Engineering, V. Uni and S. S. Canada, *Ind. Eng. Chem. Res.*, 2006, **45**, 2558–2568.

2 G. Centi and S. Perathoner, *Catal. Today*, 2009, **148**, 191–205.

3 L. Yuan and Y.-J. Xu, *Appl. Surf. Sci.*, 2015, **342**, 154–167.

4 B. AlOtaibi, S. Fan, D. Wang, J. Ye and Z. Mi, *ACS Catal.*, 2015, **5**, 5342–5348.

5 J. P. Zou, D. D. Wu, J. Luo, Q. J. Xing, X. B. Luo, W. H. Dong, S. L. Luo, H. M. Du and S. L. Suib, *ACS Catal.*, 2016, **6**, 6861–6867.

6 Y. Ji and Y. Luo, *ACS Catal.*, 2016, **6**, 2018–2025.

7 A. Corma and H. Garcia, *J. Catal.*, 2013, **308**, 168–175.

8 C. Wang, Z. Sun, Y. Zheng and Y. H. Hu, *J. Mater. Chem. A*, 2019, **7**, 865–887.

9 K. Li, B. Peng and T. Peng, *ACS Catal.*, 2016, **6**, 7485–7527.

10 X. Chen, S. Shen, L. Guo and S. S. Mao, *Chem. Rev.*, 2010, **110**, 6503–6570.

11 V. P. Indrakanti, J. D. Kubicki and H. H. Schobert, *Energy Environ. Sci.*, 2009, **2**, 745.

12 M. A. Henderson, *Surf. Sci. Rep.*, 2011, **66**, 185–297.

13 Á. Kukovecz, K. Kordás, J. Kiss and Z. Kónya, *Surf. Sci. Rep.*, 2016, **71**, 473–546.

14 S. N. Habisreutinger, L. Schmidt-Mende and J. K. Stolarczyk, *Angew. Chemie Int. Ed.*, 2013, **52**, 7372–7408.

15 B. Ohtani, *J. Photochem. Photobiol. C Photochem. Rev.*, 2010, **11**, 157–178.

16 A. Olivo, V. Trevisan, E. Ghedini, F. Pinna, C. L. Bianchi, A. Naldoni, G. Cruciani and M. Signoretto, *J. CO2 Util.*, 2015, **12**, 86–94.

17 P. Wang, G. Yin, Q. Bi, X. Huang, X. Du, W. Zhao and F. Huang, *ChemCatChem*, 2018, **10**, 3854–3861.

18 L. Wei, C. Yu, Q. Zhang, H. Liu and Y. Wang, *J. Mater. Chem. A*, 2018, 22411–22436.

19 A. Meng, S. Wu, B. Cheng, J. Yu and J. Xu, *J. Mater. Chem. A*, 2018, **6**, 4729–4736.

20 W. Wang, D. Xu, B. Cheng, J. Yu and C. Jiang, *J. Mater. Chem. A*, 2017, **5**, 5020–5029.

21 S. Xie, Q. Zhang, G. Liu and Y. Wang, *Chem. Commun.*, 2016, **52**, 35–59.

22 A. Naldoni, M. D'Arienzo, M. Altomare, M. Marelli, R. Scotti, F. Morazzoni, E. Selli and V. Dal Santo, *Appl. Catal. B Environ.*, 2013, **130–131**, 239–248.

23 T. Ochiai and A. Fujishima, *J. Photochem. Photobiol. C Photochem. Rev.*, 2012, **13**, 247–

262.

24 B. Tian, J. Zhang, T. Tong and F. Chen, *Appl. Catal. B Environ.*, 2008, **79**, 394–401.

25 T. Wang, X. Meng, G. Liu, K. Chang, P. Li, Q. Kang, L. Liu, M. Li, S. Ouyang and J. Ye, *J. Mater. Chem. A*, 2015, **3**, 9491–9501.

26 E. Bahadori, M. Compagnoni, A. Tripodi, F. Freyri, M. Armandi, B. Bonelli, G. Ramis and I. Rossetti, *Mater. Today Proc.*, 2018, **5**, 17404–17413.

27 I. Rossetti, A. Villa, M. Compagnoni, L. Prati, G. Ramis, C. Pirola, C. L. Bianchi, W. Wang and D. Wang, *Catal. Sci. Technol.*, 2015, **5**, 4481–4487.

28 I. Rossetti, A. Villa, C. Pirola, L. Prati and G. Ramis, *RSC Adv.*, 2014, **4**, 28883–28885.

29 A. Olivo, E. Ghedini, M. Signoretto, M. Compagnoni and I. Rossetti, *Energies*, 2017, **10**, 1394.

30 F. Galli, M. Compagnoni, D. Vitali, C. Pirola, C. L. Bianchi, A. Villa, L. Prati and I. Rossetti, *Appl. Catal. B Environ.*, 2017, **200**, 386–391.

31 M. Compagnoni, S. A. Kondrat, C. E. E. Chan-Thaw, D. J. Morgan, D. Wang, L. Prati, N. Dimitratos and I. Rossetti, *ChemCatChem*, 2016, **8**, 12.

32 M. Compagnoni, A. Villa, E. Bahadori, D. Morgan, L. Prati, I. Dimitratos, Nikolaos Rossetti and G. Ramis, *Catalysts*, 2018, **8**, 623.

33 I. Rossetti, A. Villa, M. Compagnoni, L. Prati, G. Ramis, C. Pirola, C. L. Bianchi, W. Wang and D. Wang, *Catal. Sci. Technol.*, 2015, **5**, 4481–4487.

34 F. Galli, M. Compagnoni, D. Vitali, C. Pirola, C. L. Bianchi, A. Villa, L. Prati and I. Rossetti, *Appl. Catal. B Environ.*, 2017, **200**, 386–391.

35 I. Rossetti, A. Villa, C. Pirola, L. Prati and G. Ramis, *RSC Adv.*, 2014, **4**, 28883–28885.

36 I. Rossetti, E. Bahadori, A. Tripodi, A. Villa, L. Prati and G. Ramis, *Sol. Energy*, 2018, **172**, 225–231.

37 H. W. Nasution, E. Purnama, S. Kosela and J. Gunlazuardi, *Catal. Commun.*, 2005, **6**, 313–319.

38 Q. Liu, Z.-X. Low, L. Li, A. Razmjou, K. Wang, J. Yao and H. Wang, *J. Mater. Chem. A*, 2013, **1**, 11563–11569.

39 S. Oros-Ruiz, R. Zanella, R. López, A. Hernández-Gordillo and R. Gómez, *J. Hazard. Mater.*, 2013, **263**, 2–10.

40 A. Villa, D. Wang, G. M. Veith, F. Vindigni and L. Prati, *Catal. Sci. Technol.*, 2013, **3**, 3036.

41 X. Z. Li and F. B. Li, *Environ. Sci. Technol.*, 2001, **35**, 2381.

42 G. M. Lari, E. Nowicka, A. Kondrat and G. J. Hutchings, *Phys. Chem. Chem. Phys.*, 2015, **17**, 23236–23244.

43 F. Zaera, *ChemCatChem*, 2012, **4**, 1525–1533.

44 X. Li, H. Liu, D. Luo, J. Li, Y. Huang, H. Li, Y. Fang, Y. Xu and L. Zhu, *Chem. Eng. J.*, 2012, **180**, 151–158.

45 E. Bahadori, A. Tripodi, A. Villa, C. Pirola, L. Prati, G. Ramis and I. Rossetti, *Catalysts*, 2018, **8**, 430.

46 L. Collado, A. Reynal, J. M. Coronado, D. P. Serrano, J. R. Durrant and V. A. De la Pe??a O'Shea, *Appl. Catal. B Environ.*, 2015, **178**, 177–185.

47 M. Tahir, B. Tahir, N. A. Saidina Amin and H. Alias, *Appl. Surf. Sci.*, 2016, **389**, 46–55.

48 I. H. Tseng, J. C. S. Wu and H. Y. Chou, *J. Catal.*, 2004, **221**, 432–440.

49 J. S. Hwang, J. S. Chang, S. E. Park, K. Ikeue and M. Anpo, *Top. Catal.*, 2005, **35**, 311–319.

50 B. Srinivas, B. Shubhamangala, K. Lalitha, P. Anil Kumar Reddy, V. Durga Kumari, M. Subrahmanyam and B. R. De, *Photochem. Photobiol.*, 2011, **87**, 995–1001.

51 A. H. Yahaya, M. A. Gondal and A. Hameed, *Chem. Phys. Lett.*, 2004, **400**, 206–212.

52 S. Gao, B. Gu, X. Jiao, Y. Sun, X. Zu, F. Yang, W. Zhu, C. Wang, Z. Feng, B. Ye and Y. Xie, *J. Am. Chem. Soc.*, 2017, **139**, 3438–3445.

53 L. Matějová, K. Kočí, M. Reli, L. Capek, V. Matějka, O. Solcová and L. Obalová, *Appl. Surf. Sci.*, 2013, **285**, 688–696.

54 M. Tahir, B. Tahir and N. A. S. Amin, *Appl. Surf. Sci.*, 2015, **356**, 1289–1299.

55 S. Delavari and N. A. S. Amin, *Appl. Energy*, 2014, **162**, 1171–1185.

56 L. Chen, M. E. Graham, G. Li, D. R. Gentner, N. M. Dimitrijevic and K. A. Gray, *Thin Solid Films*, 2009, **517**, 5641–5645.

57 G. Li, S. Ciston, Z. V. Saponjic, L. Chen, N. M. Dimitrijevic, T. Rajh and K. A. Gray, *J. Catal.*, 2008, **253**, 105–110.

58 B. Ohtani, O. O. Prieto-Mahaney, D. Li and R. Abe, *J. Photochem. Photobiol. A Chem.*, 2010, **216**, 179–182.

59 A. Kafizas, X. Wang, S. R. Pendlebury, P. Barnes, M. Ling, C. Sotelo-Vazquez, R. Quesada-Cabrera, C. Li, I. P. Parkin and J. R. Durrant, *J. Phys. Chem. A*, 2016, **120**, 715–723.

60 J. Kullgren, B. Aradi, T. Frauenheim, L. Kavan and P. De??k, *J. Phys. Chem. C*, 2015, **119**, 21952–21958.

61 W. Lin, H. Han and H. Frei, *J. Phys. Chem. B*, 2004, **108**, 18269–18273.

62 L. Liu, Y. Jiang, H. Zhao, J. Chen, J. Cheng, K. Yang and Y. Li, *ACS Catal.*, 2016, **6**, 1097–1108.

63 F. Zhang, M. Wang, X. Zhu, B. Hong, W. Wang, Z. Qi, W. Xie, J. Ding, J. Bao, S. Sun and C. Gao, *Appl. Catal. B Environ.*, 2015, **170–171**, 215–224.

64 A. Maira, J. Coronado, V. Augugliaro, K. . Yeung, J. . Conesa and J. Soria, *J. Catal.*, 2001, **202**, 413–420.

65 F. Fresno, M. D. Hernández-Alonso, D. Tudela, J. M. Coronado and J. Soria, *Appl. Catal. B Environ.*, 2008, **84**, 598–606.

66 G. Liu, N. Hoivik, K. Wang and H. Jakobsen, *Sol. Energy Mater. Sol. Cells*, 2012, **105**, 53–68.